Electronic Supplementary Material (ESI):

Redox-active Sn(II) to lead $SnFe_2O_4$ spinel as a bi-functional water splitting catalyst

Anubha Rajput,[a] Amit Anand Pandey,[a] Avinava Kundu,[a] Biswarup Chakraborty,*[a]

[a]Department of Chemistry, Indian Institute of Technology Delhi, Hauz Khas, 110016, New Delhi, India.

Email: cbiswarup@chemistry.iitd.ac.in

Table of Contents

Experimental Section

Materials and method. $SnCl_2 \cdot 2H_2O$, $FeCl_2 \cdot 4H_2O$, and NH_4OH were purchased from the Central Drug (P) House, India. Ethylene glycol was obtained from Merck, India. Nickel foam (NF) and Carbon cloth were obtained from RVL scientific, India. The chemicals were used without further purification.

Solvothermal synthesis of $SnFe_2O_4$. For the preparation of $SnFe_2O_4$, 0.017 M of $SnCl_2 \cdot 2H_2O$ and 0.034 M of $FeCl_2 \cdot 4H_2O$ were added in 25 mL ethylene glycol and were kept on stirring at room temperature. To this solution, 5 mL NH_4OH solution was added with further stirring to adjust the pH of the solution to 10. The resulting solution was transferred to a Teflon liner reactor and was kept inside a stainless-steel autoclave. The apparatus was then heated in an oven at 210 ^{o} C for 14 h. After 14 h, the autoclave was allowed to cool down to room temperature and the mixture was centrifuged. The precipitate was washed thoroughly with deionized water and ethanol and then dried in an oven at 60 ^{o} C for 2 h in air. The dried powder material was ground in an agate mortar pestle for further study.[1]

Characterization and analysis methods

The phase purity and crystalline structure of $SnFe_2O_4$ was characterized by powder X-ray diffraction on Bruker D8 Advance X-ray diffractometer equipped with Cu Kα ($K\alpha_1$ = 1.540598 Å, $K\alpha_2$ = 1.544426 Å, Kα ratio 0.5, $K\alpha_{av}$ = 1.541874Å) X-ray tubes. The diffraction pattern was recorded in the 2θ range of 10^{o} to 80^{o}. Crystallite size determination was done by Gaussian fitting of (311) peak at 2θ of 35.1^{o} giving β = 0.3. The crystallite size was calculated using the Debye-Scherrer equation[2] as follows, $Size\ (D) = 0.9\lambda/\beta cos\theta$ where, D is the crystallite size, λ is the wavelength of the X-ray source (Cu Kα 1.54 Å), β is the full width at the half-maxima. FTIR study was done to determine the type of bonding and functional groups present in the material. To do the study, a KBr palette containing the sample was made. To approximately 0.1-0.2 mg of sample, a few milligrams of KBr powder (~2 mg) was added and a palette was made. The FTIR study was done using the palette with Nicolet, Protege 460 instrument. FESEM was done to do microstructural study of the synthesized nanomaterial. Alongside, Energy dispersive X-ray spectroscopy (EDX) for mapping and elemental analysis was also done. The aforementioned techniques were done on as prepared sample and the sample deposited on NF before and after electrocatalysis through JSM-IT300HR, JEOL instrument. The high resolution transmission electron microscopy (HRTEM), and selected area electron diffraction (SAED) patterns were done using Thermo-fisher Technie microscope working at accelerating voltage 200 kV. The TEM grid preparation was done in HPLC grade acetone (Merck, India) on the 200-mesh carbon coated Cu grids [TED PELLA, INC.]. The surface study of the as synthesized material was done to find out the composition of surface and the oxidation state of the chemical species present on the material surface with the help of X-ray photoelectron spectroscopy (XPS). The measurement was done using ESCA+, omicron nanotechnology, Oxford Instrument Germany, equipped with aluminium monochromator with aluminium source (Al Kα radiation hν =1486.7eV). The operational voltage and current of the instrument are at 15 kV and 15 mA respectively.

Preparation and deposition of catalyst ink on the electrode surface. Three dimensional and porous network like nickel foam (NF) was chosen as electrode substrates for catalyst deposition. The following steps were sequentially employed to prepare a catalyst ink and subsequently to deposit it on NF: (i) The sheet of NF was cut in several pieces of dimension 1 x 2 cm^2. It was then washed ultrasonically in 0.1 N HCl followed by washing twice with milli-Q water and once with acetone. The electrodes were then dried at 50 ^{o}C overnight in an oven. (ii) To prepare the ink, Nafion was used as a medium to disperse the catalyst in aqueous medium. Nafion is a conductive, sulfonated tetrafluoroethylene-based fluoropolymer which binds the catalyst particles on the electrode surface.

Nafion was diluted to 1.0 wt% in ethanol and 50 mg catalyst powder was added into it. The mixture was homogenized by sonicating it for 10 minutes at room temperature. (iii) The prepared ink was drawn in a pipette and was deposited dropwise on pre-cleaned NF surface. The 1x1 cm^2 surface area was covered with the ink after which the electrode was left to dry at room temperature overnight.

Electrochemical measurement. To study the electrocatalytic activity, a potentiostat (Gamry Interface 1010E) instrument controlled by Echem Analyst™ Software was used for electrochemical measurements and the Origin software was used to further analyze the data. The electrochemical study was done typically in a three-electrode system using 1 M KOH electrolyte (pH 13.6). Among the three electrodes, NF loaded with catalyst was used as a working electrode (WE), A platinum coil electrode was used as a counter electrode (CE) and a Hg/HgO was used as a reference electrode (RE). The working potential has been converted to RHE using the following relation:

$E_{RHE} = E_{Hg/HgO} + 0.098\ V + (0.059 \times pH)\ V$

The CV and LSV were measured to study the electrochemical OER. The electrochemical measurement (CV and LSV) were done with a manual iR compensation (R = resistance of solution including the test electrode) of 85%, in which the value of uncompensated resistance was obtained from the impedance study. Oxygen evolution reaction (OER) and hydrogen evolution reaction (HER) were studied at a scan rate of 1 mV s^{-1}. To determine the electrochemical double layer capacitance (C_{dl}) of the catalyst, different scan rates (10, 25, 50, 100, 150 and 200 mVs^{-1}) were used in the potential range 0.8953 V to 0.9953 V (vs. RHE). Tafel slopes are calculated from the slope of the overpotential (η) versus the logarithm of current density (log *j*) plot and the slope was determined from the kinetically controlled region of the curve. The Tafel slope was calculated according to the Tafel equation:[3]

$$\eta = b\log j + a \qquad \text{Equation S1}$$

where η is the overpotential (V), *j* is the current density (mA cm^{-2}), and b is the Tafel slope (mV dec^{-1}).

The chronoamperometry (CA) study was done to study the stability of the catalyst i.e., its durability without substantial loss in activity. CA was performed in 1 M KOH, for 22 h at a constant potential. Electrochemical impedance spectroscopy (EIS) was recorded in a frequency region of 100 mHz to 1 MHz and the obtained data is plotted as Re Z vs Im Z (Nyquist plot).

The TOF indicate the moles of oxygen evolved from per moles of total metal content per second (s^{-1}). For electrocatalyst, TOF was calculated from the following equation.[4]

$$TOF\ (s^{-1}) = \frac{j \times A}{Z \times F \times n} \qquad \text{Equation S2}$$

Where, j = OER current density, A = geometrical electrode surface area, F = 96485.33289 C mol^{-1}, Z = 4 electron transfer in overall reaction, and n = mole number of transition metal.

The Faradic efficiency of $SnFe_2O_4$ for OWS was tested in 1 M KOH in a two electrode cell having $SnFe_2O_4$/NF as cathode as well as the anode. The OER activity was tested for 150 mins at a constant current density of 10 mA cm^{-2}. The oxygen gas evolved at the anode and hydrogen gas evolved at the cathode was quantified by the change in volume of electrolyte.

Surface concentration of redox species from redox peaks of HER CV (Figure S23 b) cycle was calculated in following manner:[5]

Integrated area of redox peak for Fe^{3+} to Fe^{2+} = 0.129 × 10^{-3} VA
Corresponding charge (Q) = 0.00013 VA / 0.01 Vs^{-1}
= 0.013 As (As = C)

No. of electrons transferred = 0.013 C / 1.602 ×10^{-19} C = 0.0081 ×10^{19}

Since, the reduction of Fe^{3+} to Fe^{2+} is a 1 electron transfer process, the number electrons transferred is equal to the number of surface active sites.
Hence, number of Fe participating is = 8.1 ×10^{18}
Similarly, the number of Sn participating in HER calculated from integrated area of redox peak for Sn^{2+} to Sn^{0} is 10^{17}.

Table S1. Electrocatalytic HER, OER, and OWS performance of $SnFe_2O_4$, noble metal catalysts and spinel ferrites reported so far.

Material	Substrate	Mass loading (mg cm^{-2})	Electrolyte	η_{OER}[a] (mV)	η_{HER}[b] (mV)	Cell potential (V)[a]	Reference
$SnFe_2O_4$	NF	5.5	1 M KOH	263	151	1.69	This work
Fe_3O_4	NF	5.7	1 M KOH	303	163	-	This work
IrO_2	NF	8.9	1 M KOH	287	-	-	This work
RuO_2	NF	8.7	1 M KOH	284	-	-	This work
Pt	Pt	-	1 M KOH	-	39		This work
$NiFe_2O_4$	GC	0.35	1 M KOH	380	-		*6*
$NiFe_2O_4$	GC	1.4	1 M KOH	410	-		*7*
$NiFe_2O_4$	GC	0.21	1 M KOH	262	-		*8*
$NiFe_2O_4$	GC	0.56	1 M KOH	350	-		*9*
$CoFe_2O_4$	CP	0.2	1 M KOH	1.51[c]	-		*10*
$CoFe_2O_4$	NF	2	1 M KOH	253	-		*11*
$NiFe_2O_4$	GC	0.12	O_2 saturated 1 M KOH	347	-		*12*
$CoFe_2O_4$	GC	-	O_2 saturated 1 M KOH	430	-		*13*
$MgFe_2O_4$	GC	1.5	1 M KOH	1.09[c]	402	-	*14*
$SrFe_2O_4$	GC	0.13	1 M KOH	312	-		*15*
$CuFe_2O_4$	SS		6 M KOH	290	241	-	*16*
$ZnFe_2O_4$	NF	0.28	1 M KOH	232	-		*17*
$CoFe_2O_4$	CS	-	1 M KOH	-	270		*18*
$CuFe_2O_4$	CS	-	1 M KOH	-	320		*18*
$NiFe_2O_4$	CS	-	1 M KOH	-	420		*18*
$ZnFe_2O_4$	CS	-	1 M KOH	-	520		*18*
$NiFe_2O_4$	NF	-	1 M KOH	269	153	1.72	*19*
$CoFe_2O_4$	CC	2	1 M KOH	392	255	-	*20*
$NiFe_2O_4$	CC	2	1 M KOH	340	201	1.78	*20*
$NiFe_2O_4$	CP	2	1 M KOH	381	264	-	*21*
Fe_3O_4	CC	2	1 M KOH	432	359	-	*20*
Fe_3O_4	GC	-	Ar purged 1 M NaOH	449[d]	-		*22*

[a]@10 mA cm^{-2}, [b]@-10 mA cm^{-2}, NF = Nickel foam; GC = Glassy carbon electrode; CS = Copper sheet; CP = Carbon paper; CC = Carbon cloth, [c] in V, [d]@10 mA cm^{-2}

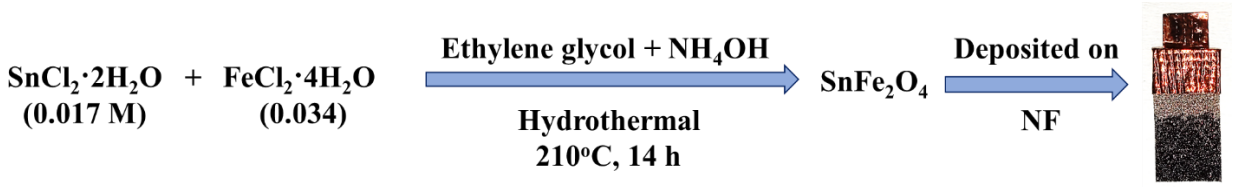

Scheme S1. Synthetic procedure for the preparation of crystalline $SnFe_2O_4$ and subsequent electrode preparation.

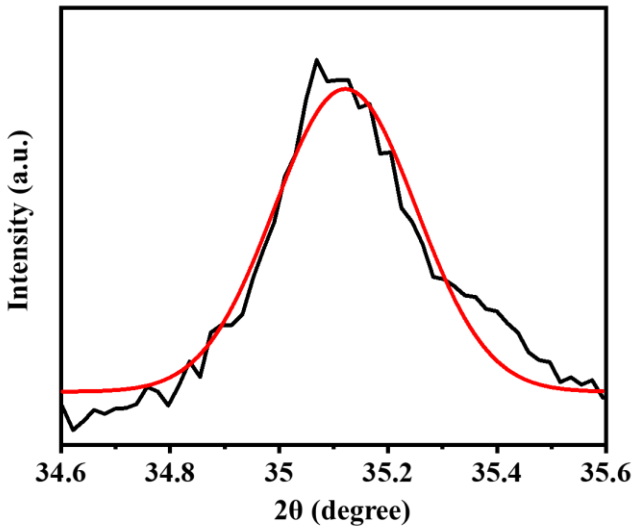

Figure S1. Crystallite size determination for $SnFe_2O_4$ from PXRD through the fitting of (311) plane using Debye- Scherrer's equation (details described in the experimental; β is the full width at the half-maxima).

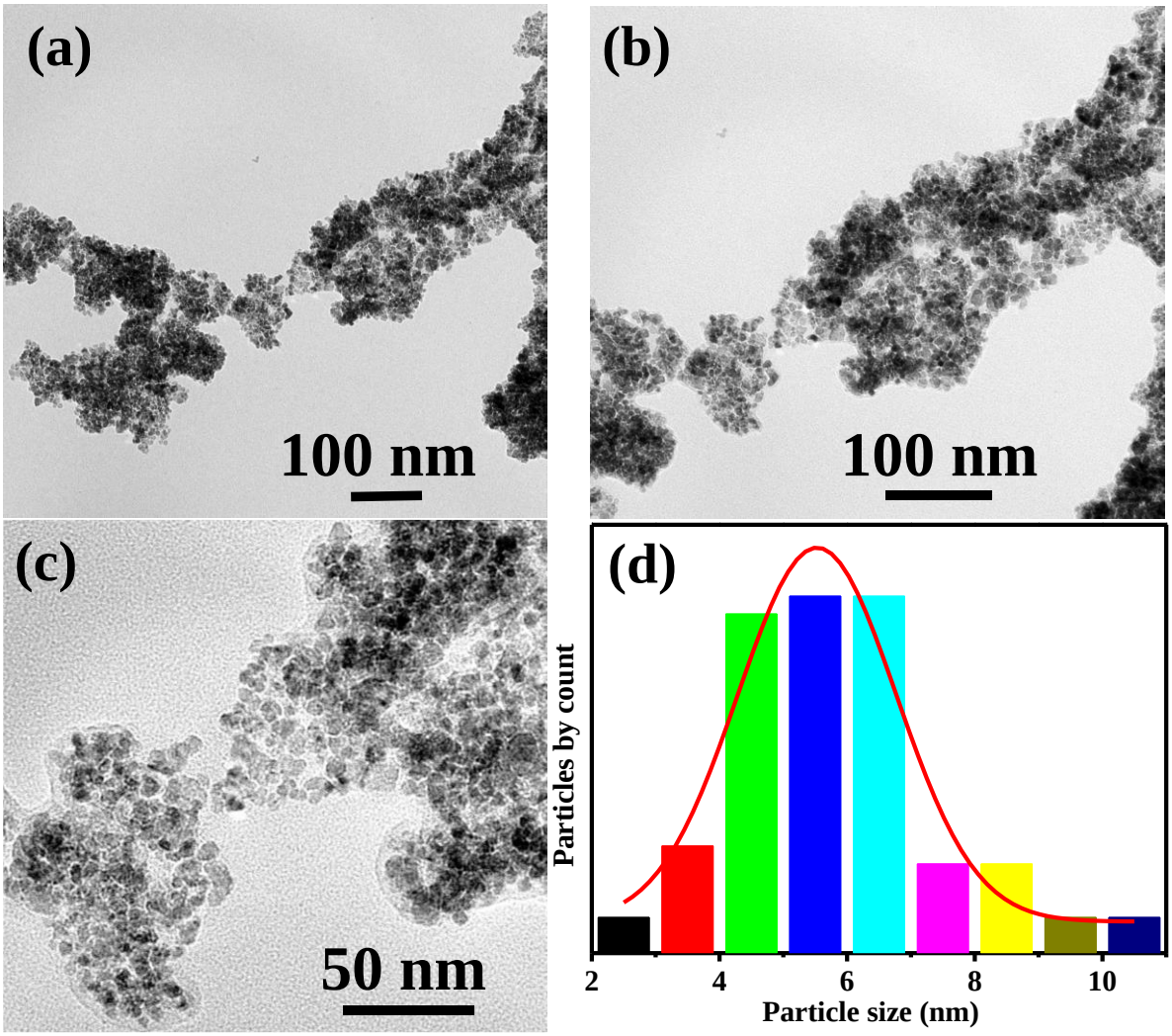

Figure S2. (a-c) HRTEM image of as-synthesized $SnFe_2O_4$ nanoparticles at different magnifications confirming the granular morphology of the catalyst. (d) Histogram showing the size distribution of the nanoparticles.

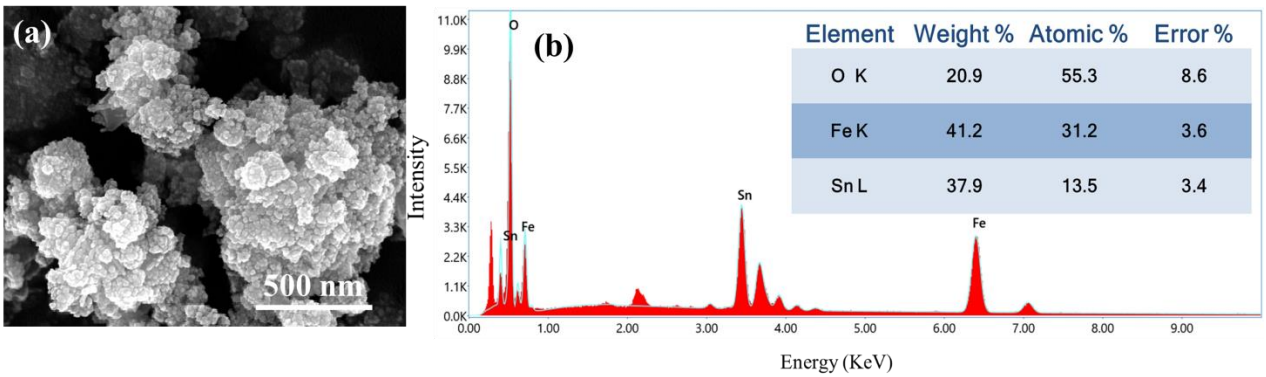

Figure S3. (a) FESEM images of as-synthesized $SnFe_2O_4$ and (b) EDX spectrum of as-synthesized $SnFe_2O_4$. Inset shows the ratio of elements present on the surface of the as synthesized catalyst.

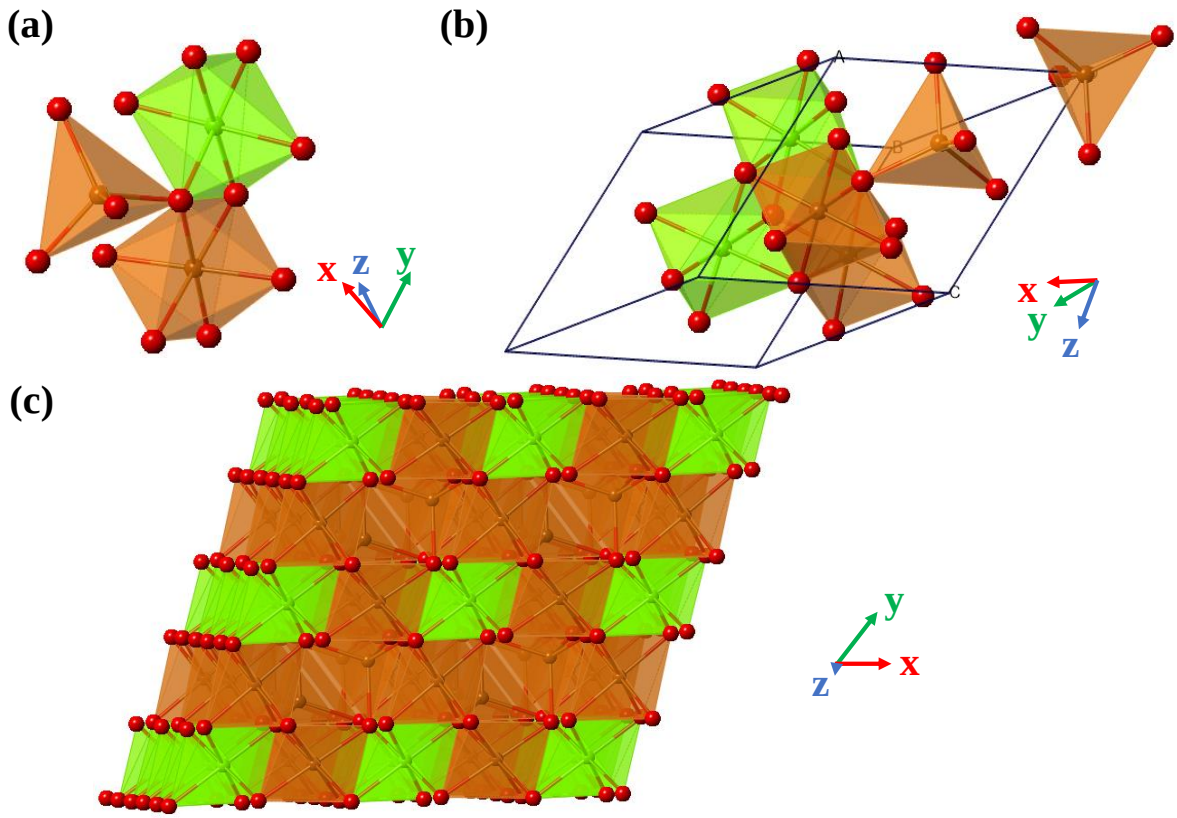

Figure S4. (a) The polyhedral presentation of the octahedral and tetrahedral units of iron and tin. (b) A single unit cell of $SnFe_2O_4$ (c) The extended polyhedral representation of $SnFe_2O_4$. Colour code: Brown polyhedral = Iron; green polyhedral = Tin; red spheres = oxygen.

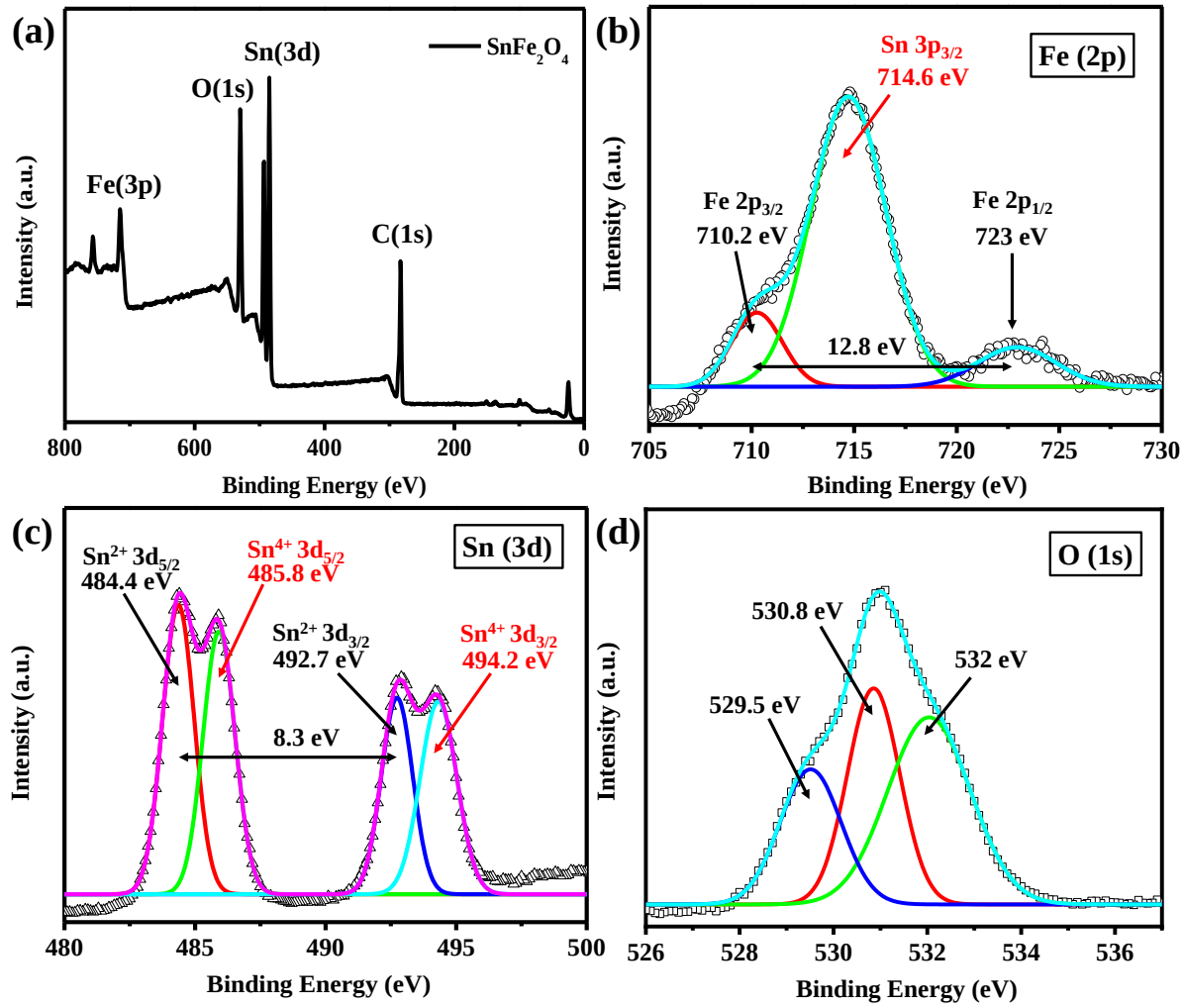

Figure S5. (a) Core level XPS spectra of $SnFe_2O_4$. High resolution scans with deconvolution for (b) Fe 2p (c) Sn 3d, and (d) O 1s.

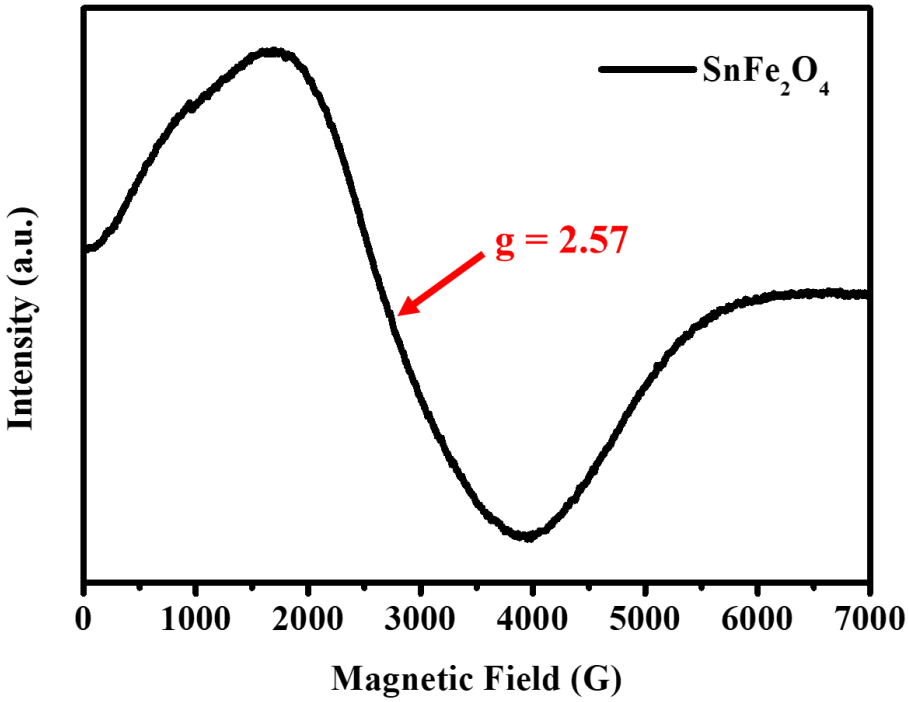

Figure S6. X-band EPR spectrum of the as-synthesized $SnFe_2O_4$ at 77 K.

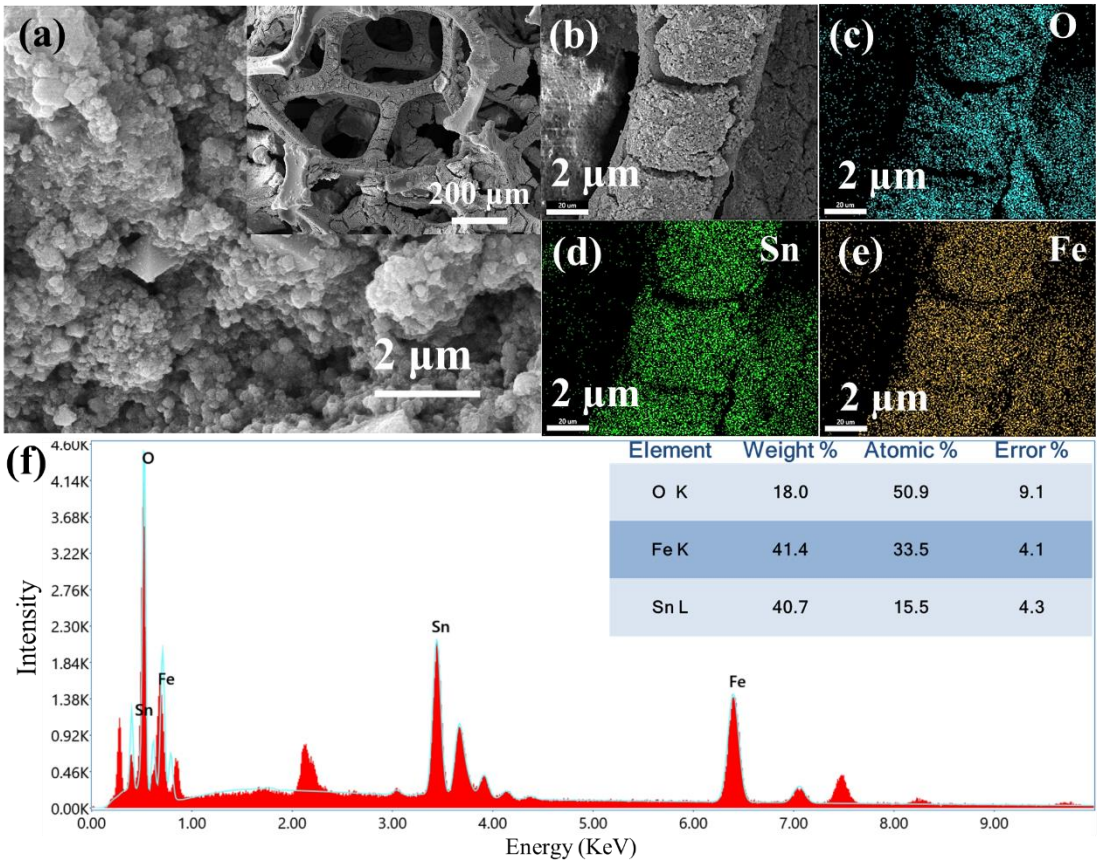

Figure S7. (a) FESEM images of as-deposited $SnFe_2O_4$ on NF and (b-e) SEM-EDX elemental mapping showing the homogeneous distribution of (c) O, (d) Sn, and (e) Fe in as-deposited $SnFe_2O_4$ powder. (f) EDX spectrum of as-deposited $SnFe_2O_4$ on NF. Inset shows the ratio of elements present on the surface of the as-deposited $SnFe_2O_4$ catalyst.

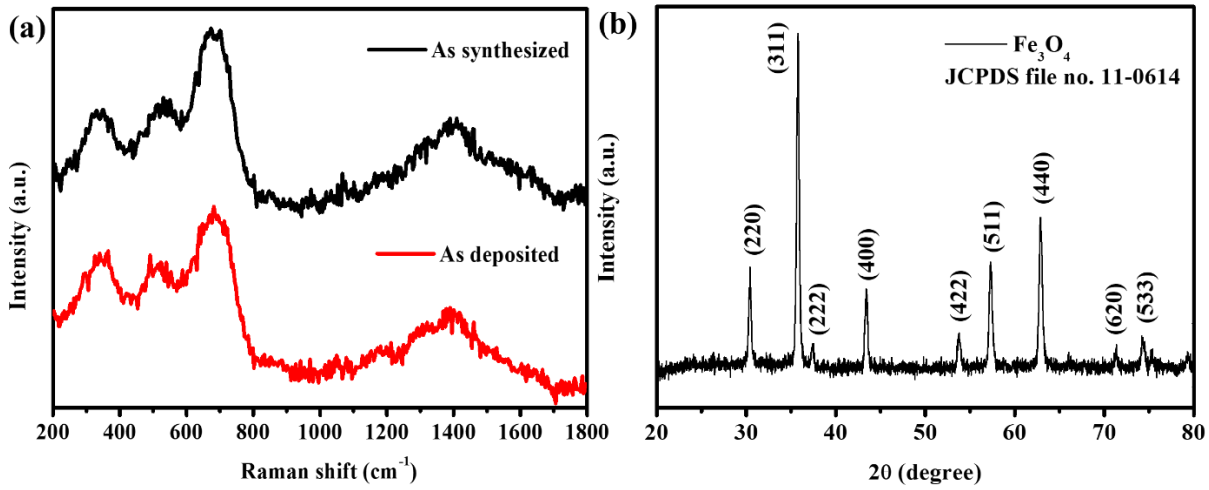

Figure S8. (a) Raman spectra of the as deposited $SnFe_2O_4$ on NF (red curve) and as synthesized (black curve). (b) PXRD pattern of as-prepared Fe_3O_4, used as a reference material.[23]

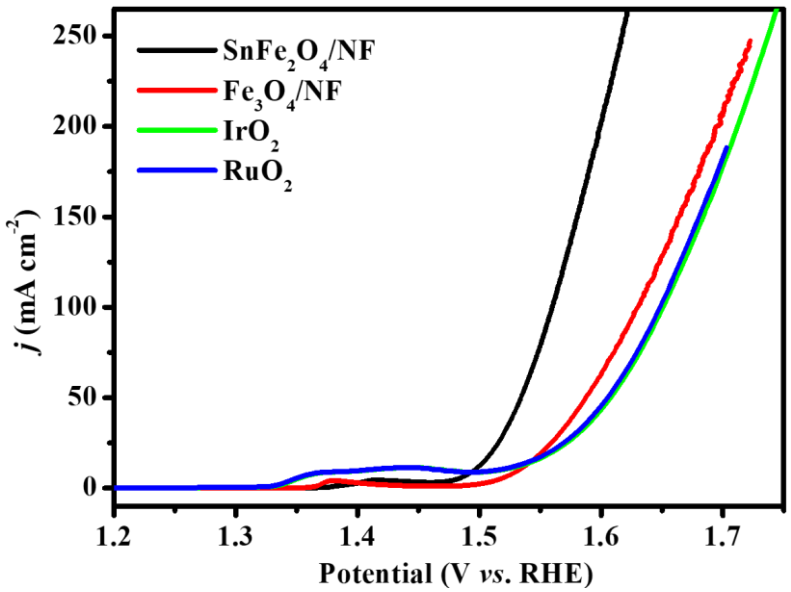

Figure S9. Polarograms from LSV study for OER with $SnFe_2O_4$/NF in comparison with Fe_3O_4 and other noble metal based catalysts like RuO_2 and IrO_2. A broad redox peak was observed for RuO_2 and IrO_2 in the low potential region (1.35 to 1.55), while the better OER activity can be observed for $SnFe_2O_4$ above 1.5 V (vs RHE).

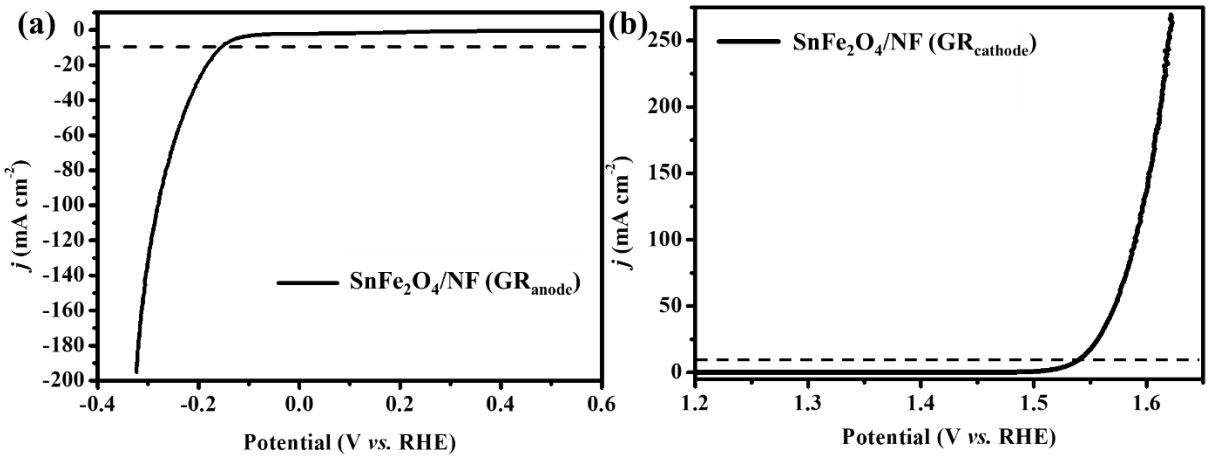

Figure S10. (a) HER LSV polarogram of $SnFe_2O_4$/NF using graphite rod (GR) as the counter electrode (CE). (b) OER LSV polarogram of $SnFe_2O_4$/NF using graphite rod as the counter electrode. The leaching of the Pt CE can occur to the electrolyte which can further be re-adsorbed on catalyst and/or working electrode surface and might influence the catalyst's electrochemical activity. Therefore, to eliminate the influence of the Pt counter electrode on the catalyst's activity, GR was used as a CE.[3]

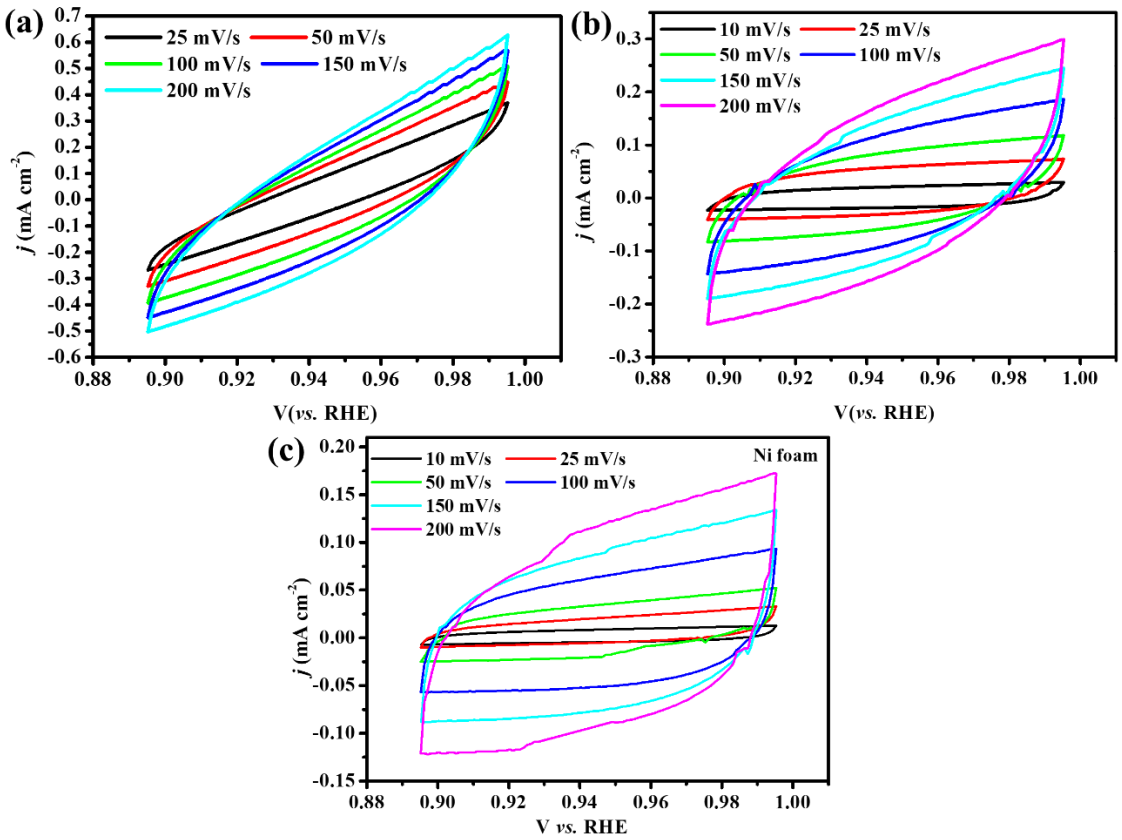

Figure S11. ECSA analysis from the CV scans in a non-Faradaic potential range of the as-prepared electrodes (a) $SnFe_2O_4$/NF, (b) Fe_3O_4/NF and (c) bare NF in 1 M KOH. Half of the differences in current density variation ($\Delta J = (J_{cathodic}-J_{anodic})/2$) at a potential of 0.94 V (vs. RHE) plotted against scan rate fitted to a linear regression enables the determination of double-layer capacitance (C_{dl}).

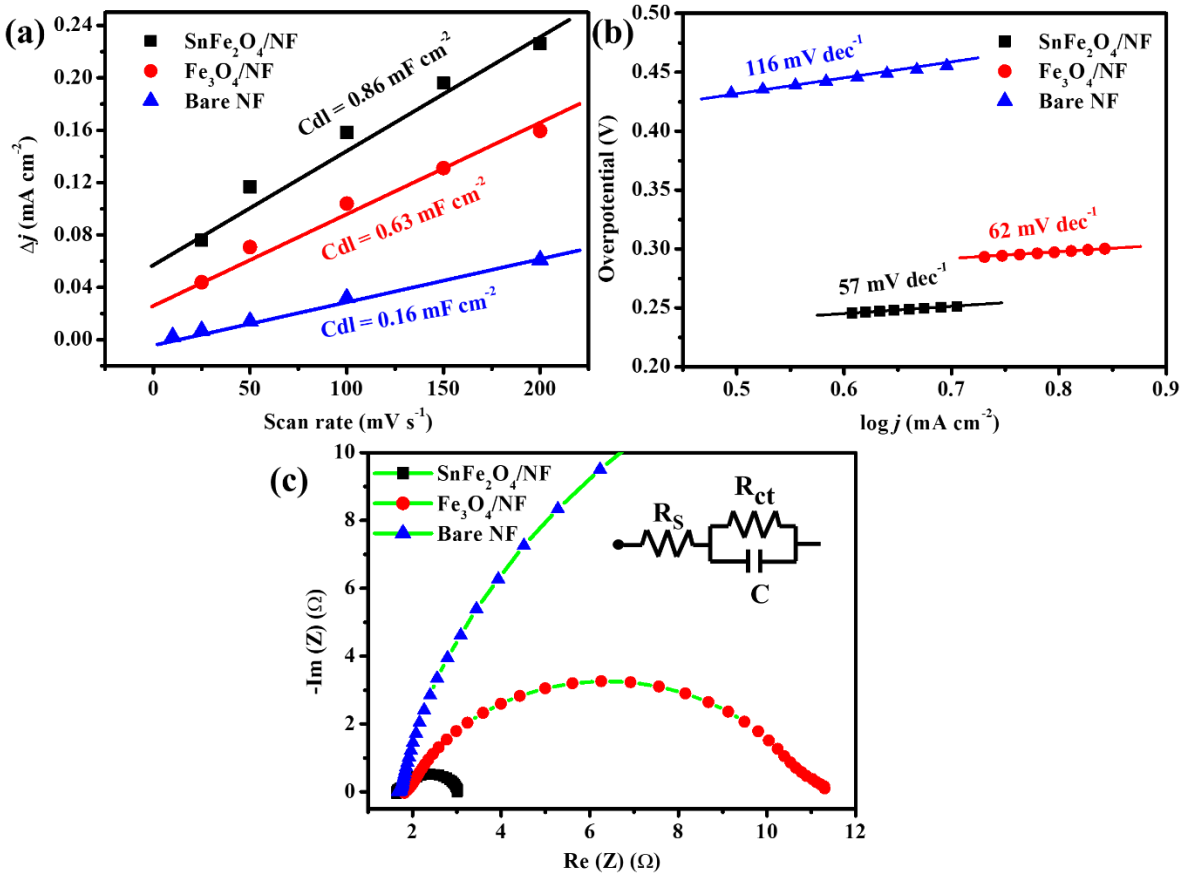

Figure S12. (a) C_{dl} values of $SnFe_2O_4$/NF, Fe_3O_4/NF, and bare NF calculated from the slopes of the linear fitting of Δj (mA cm^{-2}) versus scan rate (mV s^{-1}). (b) The Tafel slope obtained from the LSV curves for the $SnFe_2O_4$/NF, Fe_3O_4/NF, and bare NF. (c) Nyquist plots for $SnFe_2O_4$/NF, Fe_3O_4/NF, and bare NF from the data obtained from EIS study and the corresponding circuit diagram in the inset.

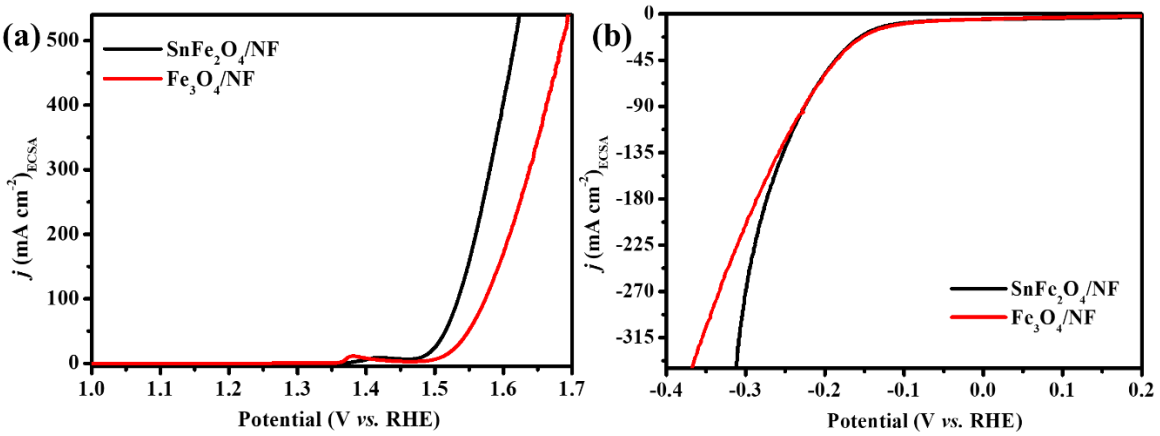

Figure S13. (a) ECSA normalized OER activity of $SnFe_2O_4$/NF, and Fe_3O_4/NF in 1 M KOH. (b) ECSA normalized HER activity of $SnFe_2O_4$/NF, and Fe_3O_4/NF in 1 M KOH.

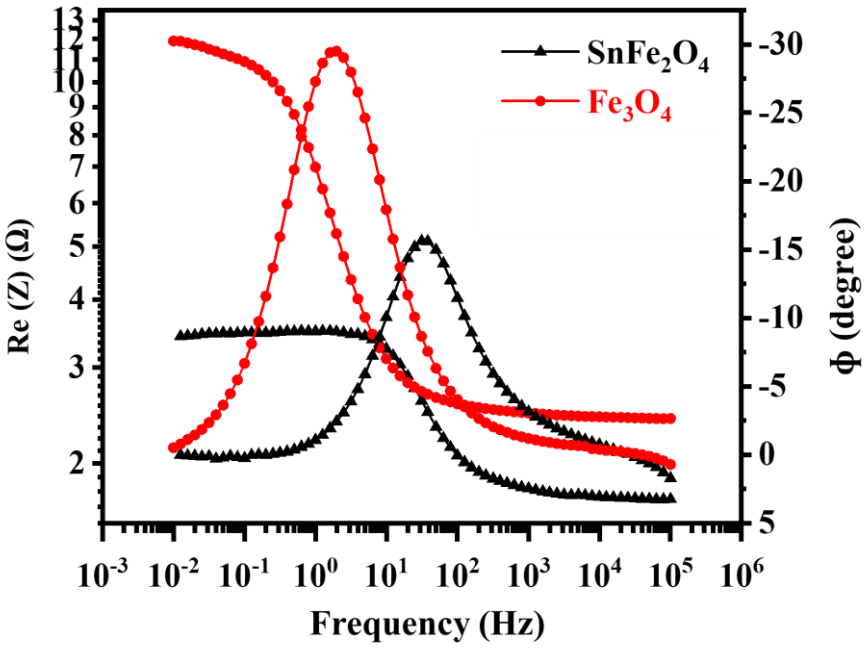

Figure S14. Bode plot, where the modulus Z and phase angle ϕ are plotted against the modulation frequency.

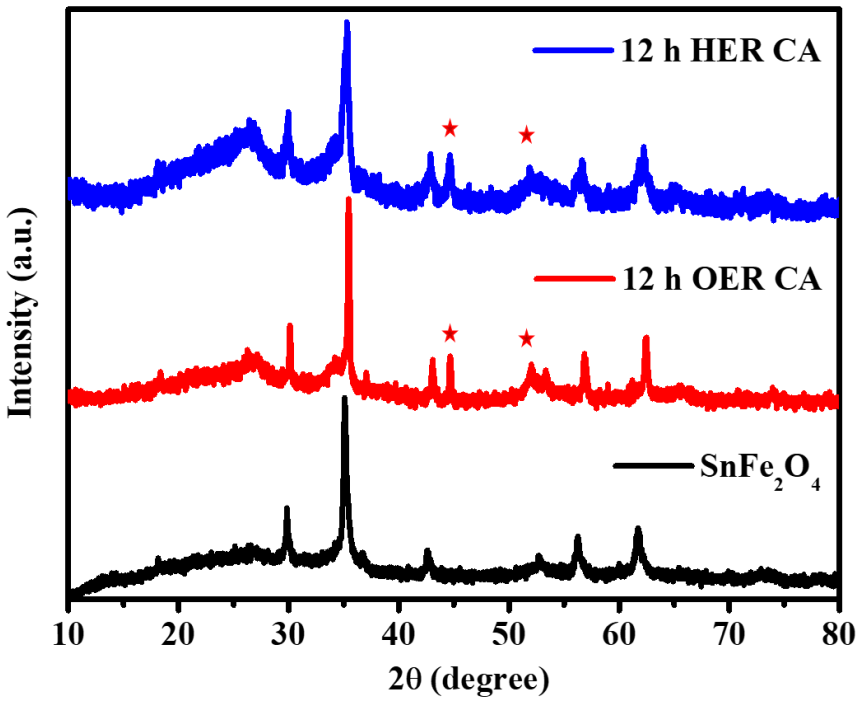

Figure S15. PXRD of as synthesized $SnFe_2O_4$, after OER-CA and after HER-CA for 12 h. (* peaks are for Ni metal from the Ni foam.)

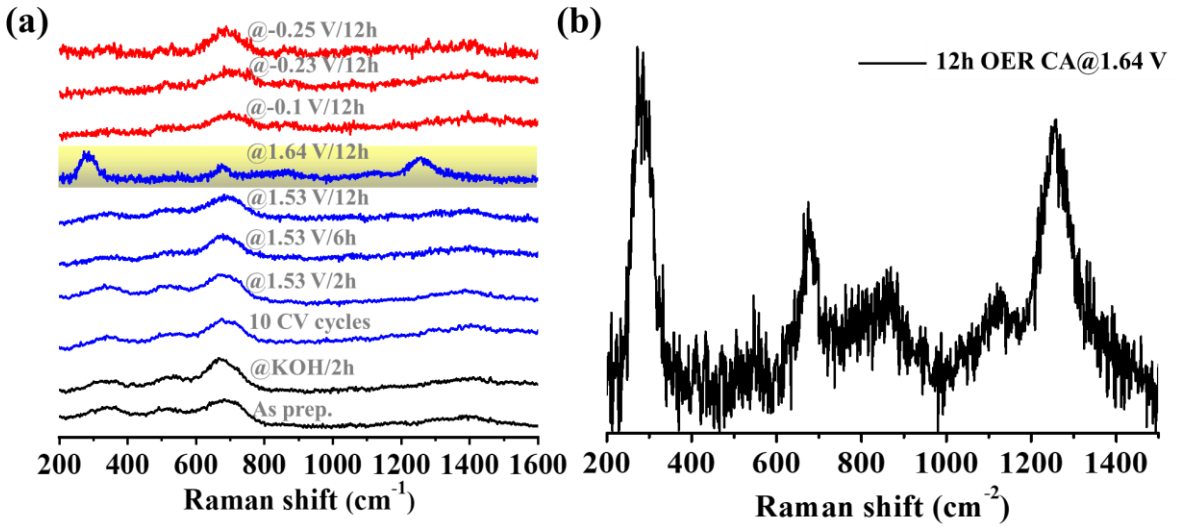

Figure S16. (a) Raman spectra of the $SnFe_2O_4$/NF electrode under different potential conditions. (b) Raman spectrum after 12 h OER CA at 1.64 V (vs. RHE).

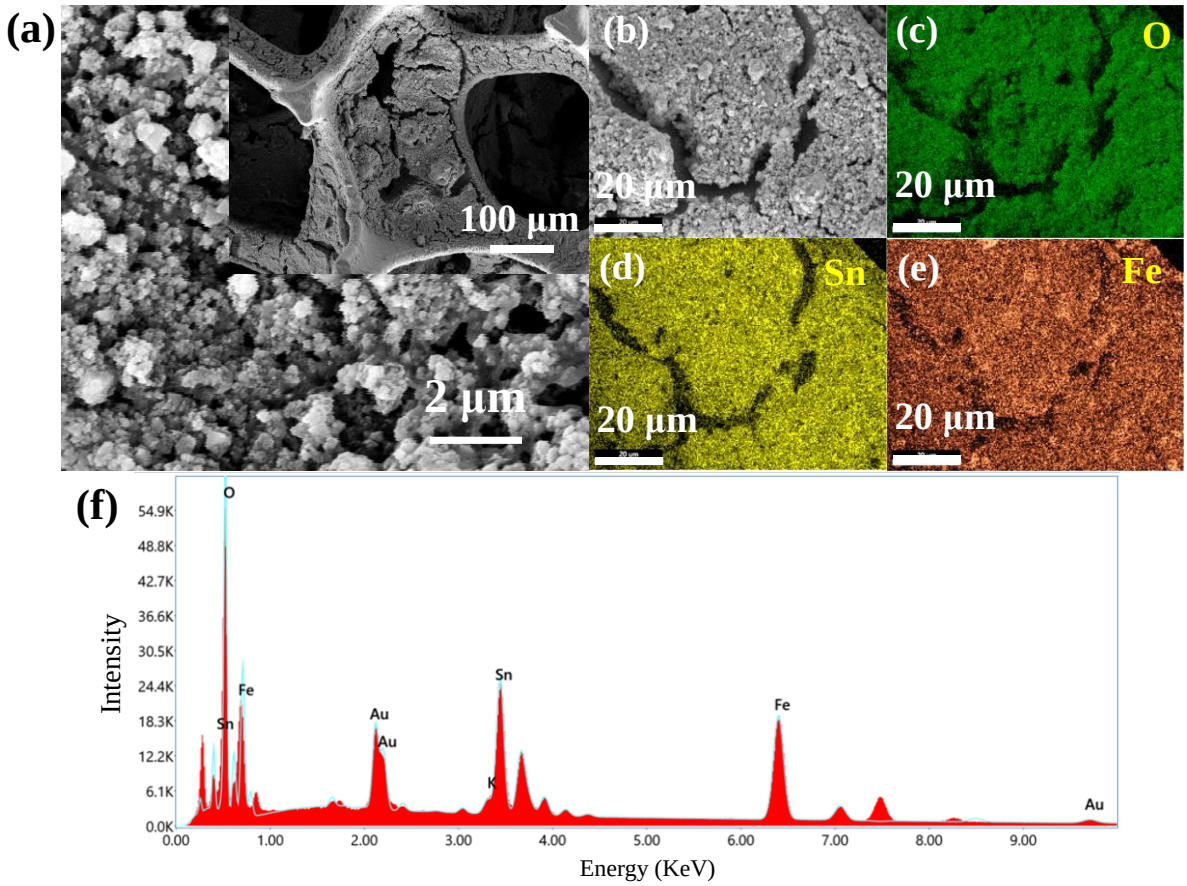

Figure S17. Microscopic FESEM characterization of $SnFe_2O_4$/NF after 12 h HER CA (a) The high resolution image depicting the grain-like morphology of the $SnFe_2O_4$ material and inset showing portion of $SnFe_2O_4$/NF electrode (b-e) SEM-EDX elemental mapping showing the homogeneous distribution of (c) O, (d) Sn, (e) Fe on NF surface. (f) The EDX mapping showing the relative ratio of elements present on the surface. The presence of K and Au is due to the unwashed KOH and Au sputtering respectively.

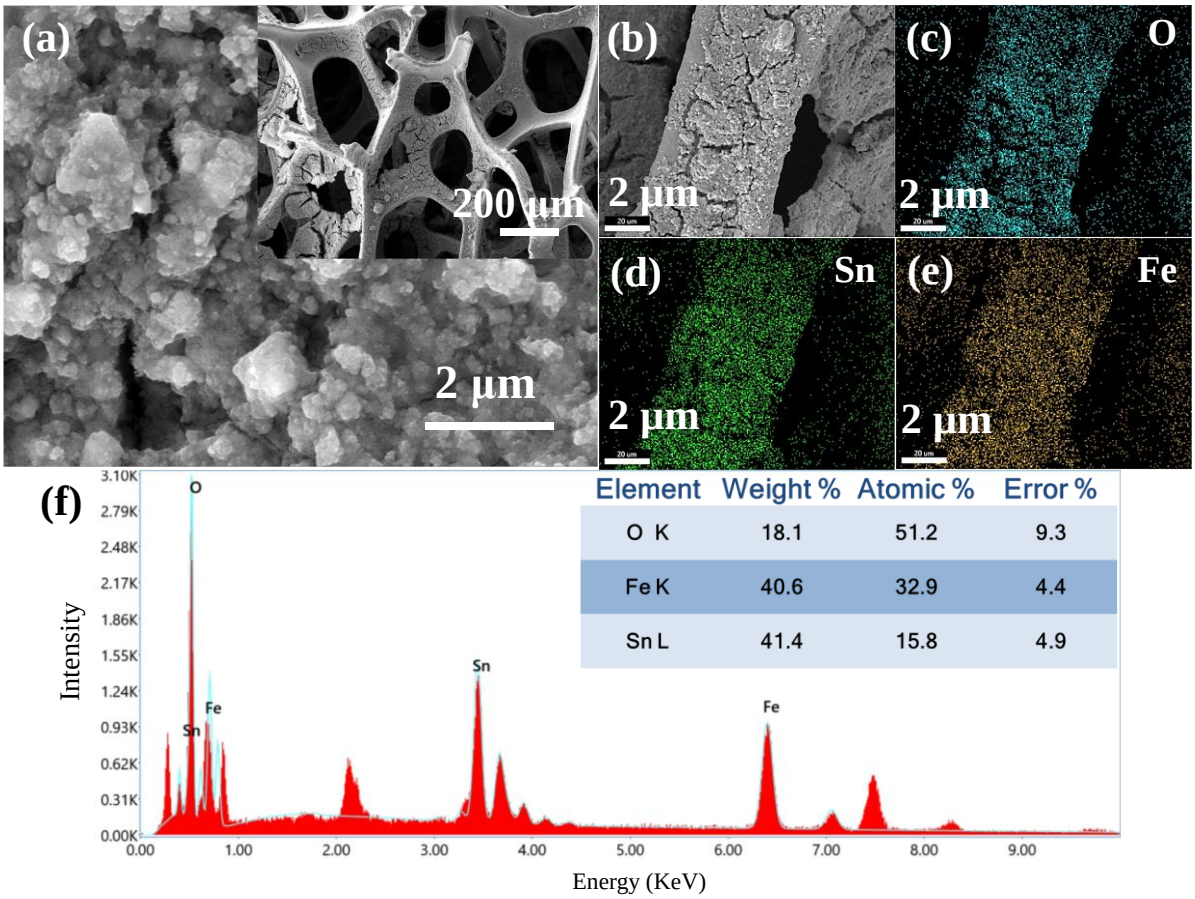

Figure S18. Microscopic FESEM characterization of $SnFe_2O_4$/NF after 12 h OER CA (a) The high resolution image depicting the grain-like morphology of the $SnFe_2O_4$ material and inset showing portion of $SnFe_2O_4$/NF electrode (b-e) SEM-EDX elemental mapping showing the homogeneous distribution of (c) O, (d) Sn, (e) Fe on NF surface. (f) The EDX mapping showing the relative ratio of elements present on the surface. The undefined peaks correspond to K and Au due to the unwashed KOH and Au sputtering respectively.

Table S2. Data file of the ICP-MS study of the electrolyte at different potentials for during 12h HER and OER CA of $SnFe_2O_4$/NF electrode. The HER study was done at -1.05 and -1.2 V (vs. Hg/HgO) and OER study was done at 0.6 and 0.7 V (vs. Hg/HgO).

					56 Fe [He]		118 Sn [He]	
Data File	Acq. Date-Time	Type	Level	Sample Name	Conc. [ppb]	Conc. RSD	Conc. [ppb]	Conc. RSD
007CALB.d	02-08-2022 11:44	CalBlk	1	BLANK	0	N/A	0	N/A
008CALS.d	02-08-2022 11:47	CalStd	2	10 ppb	12.238	5.3	9.889	5.3
009CALS.d	02-08-2022 11:51	CalStd	3	20 ppb	21.604	2.4	20.495	0.9
010CALS.d	02-08-2022 11:54	CalStd	4	50 ppb	49.992	1.9	48.411	1.3
011CALS.d	02-08-2022 11:58	CalStd	5	100 ppb	103.806	1	97.872	0.9
012CALS.d	02-08-2022 12:02	CalStd	6	200 ppb	199.73	1.7	201.417	2.2
033SMPL.d	02-08-2022 13:16	Sample		Anubha HER -1.2V 10x	16.315	1.6	72.212	5.3
034SMPL.d	02-08-2022 13:20	Sample		Anubha HER -1.05V 10x	11.938	5.5	54.608	5
035SMPL.d	02-08-2022 13:24	Sample		Anubha SF 0.7V 10x	3.565	7.2	60.604	0.8
036SMPL.d	02-08-2022 13:27	Sample		Anubha SF 0.6V 10x	3.007	9.9	49.845	2

Table S3. The weight % of Sn/Fe in electrolyte during HER and OER CA leached from $SnFe_2O_4$/NF was investigated during long-term CA for 12 h. 5.5 mg $SnFe_2O_4$ was loaded on the 1x1 cm^2 NF surface which is equivalent to 0.0186 mmole of $SnFe_2O_4$. Volume of the electrolyte (1 M KOH) was 40 mL. Now, 100 % leaching of Sn and Fe from the NF surface to electrolyte would give rise to 0.0186 mili-moles of Sn and 0.0372 mili-moles of Fe in 40 mL 1 M KOH. Fe and Sn concentration (in ppb) in the electrolyte obtained from the ICP-MS was calculated according to the dilution factor (10x provided in the data sheet). This ppb concentration was converted to the mg of atom (Fe and Sn) present in 40 mL electrolyte solution. The obtained concentration of Fe and Sn on subsequent division with the respective species' molar mass gave an idea about the amount of Fe and Sn leached into the solution after CA at respective potentials. Hence, the table provided below provides the real time Fe and Sn leaching.

	Electrolyte					
Potential (V vs. RHE)	**Fe (ppb)**	**Sn (ppb)**	**Fe in 40 mL KOH (mg)**	**Sn in 40 mL KOH (mg)**	**Fe (%) leached**	**Sn (%) leached**
-0.1	119.4	546.1	0.0048	0.0218	2.31×10^{-4}	1×10^{-3}
-0.25	163.1	722.1	0.00652	0.0288	3.1×10^{-4}	1.3×10^{-3}
1.65	30.0	498.5	0.0012	0.02	0.58×10^{-4}	0.9×10^{-3}
1.55	35.0	606.0	0.0014	0.024	0.67×10^{-4}	1.08×10^{-3}

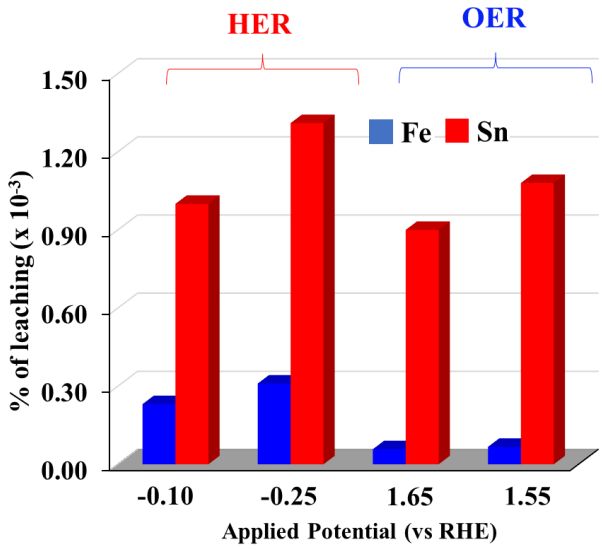

Figure S19. Histogram showing the leaching of Fe and Sn at different potentials, under OER and HER conditions.

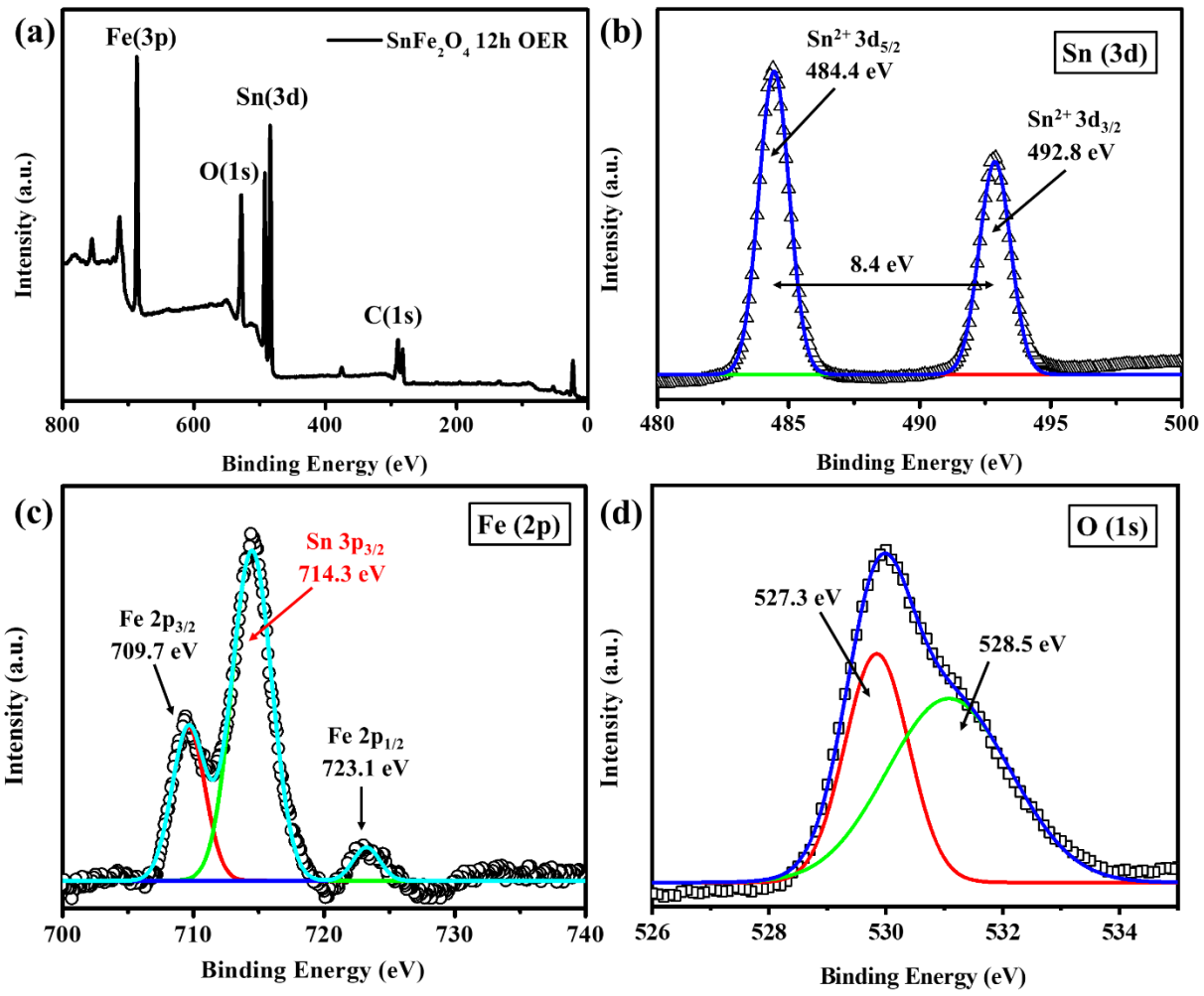

Figure S20. XPS survey spectra of the sample isolated from $SnFe_2O_4$/NF after 12 h of OER-CA. (a) Core level XPS spectra of $SnFe_2O_4$ after 12 h OER CA. High resolution scans with deconvolution for (b) Sn 3d, (c) Fe 2p, and (d) O 1s.

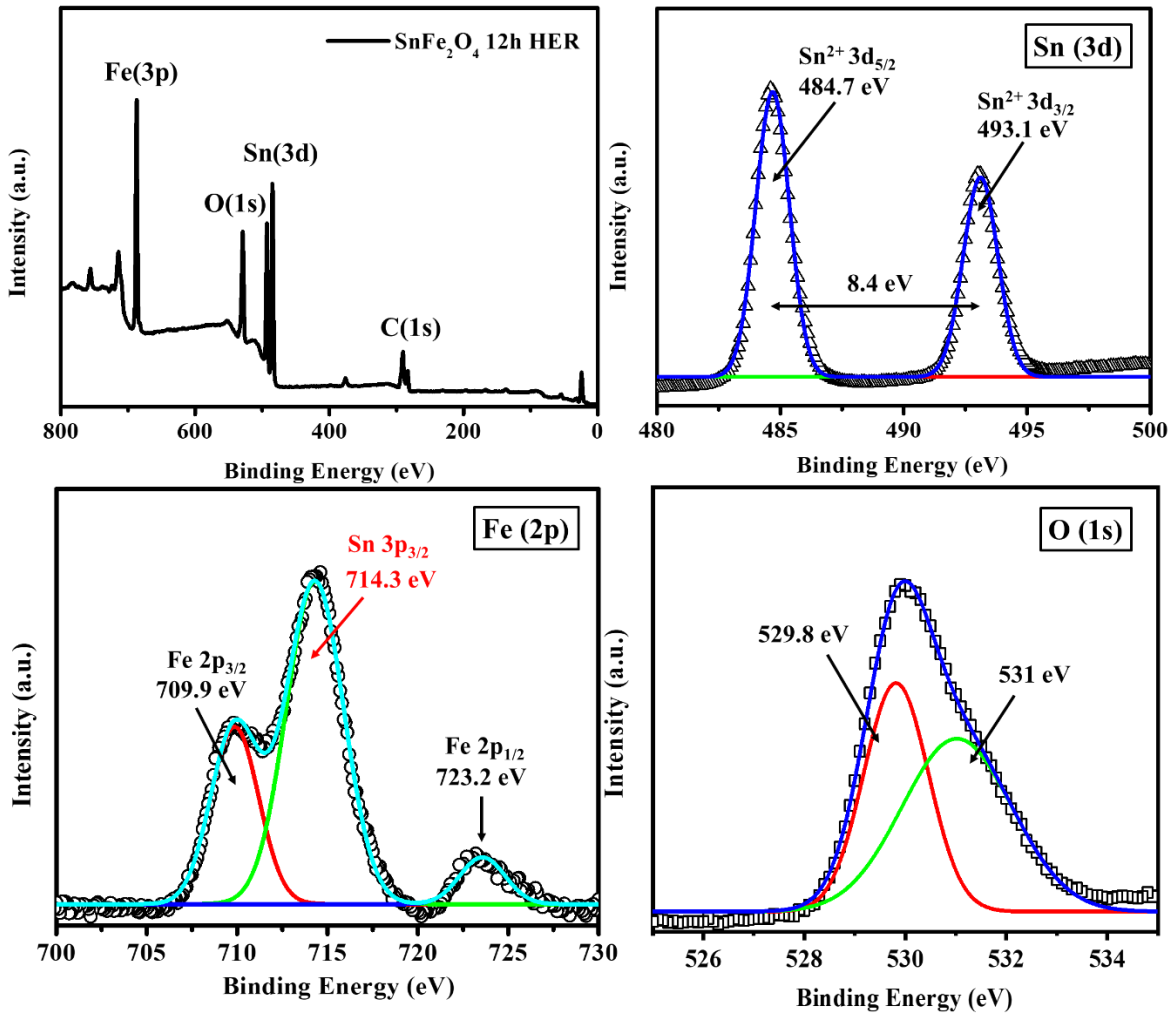

Figure S21. XPS survey spectra of the sample isolated from $SnFe_2O_4$/NF after 12 h of HER-CA. (a) Core level XPS spectra of $SnFe_2O_4$ after 12 h HER CA. High resolution scans with deconvolution for (b) Sn 3d, (c) Fe 2p, and (d) O 1s.

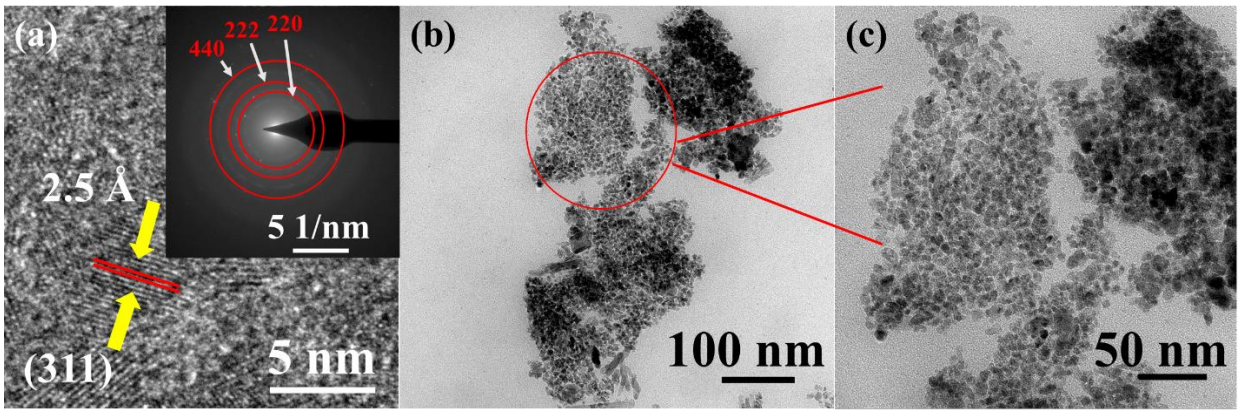

Figure S22. HRTEM image of $SnFe_2O_4$ after 12h OER. (a) HRTEM image of a selected particle showing the d(311) fringes. Inset shows the SAED pattern showing well defined rings. (b,c) The HRTEM images at different magnifications confirming the granular morphology of the catalyst along with some rod like structures.

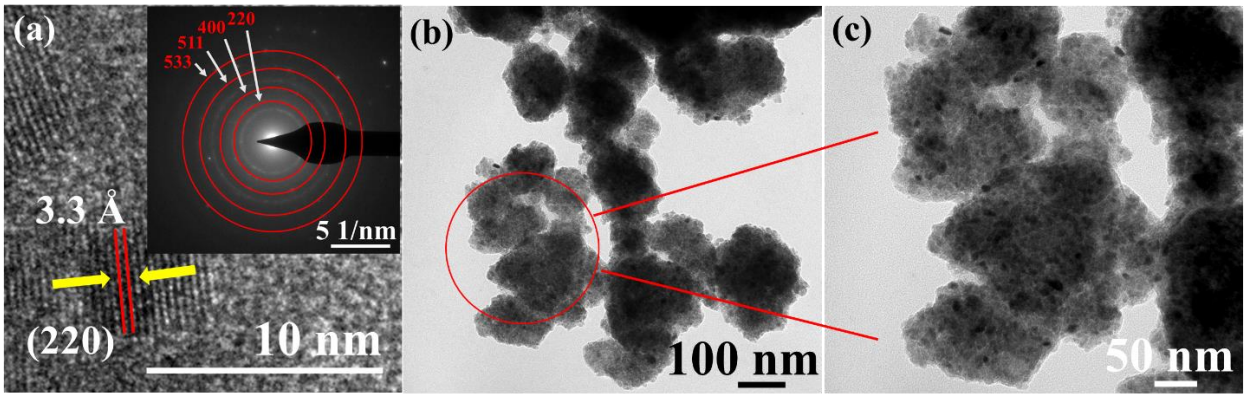

Figure S23. HRTEM image of $SnFe_2O_4$ after 12h HER. (a) HRTEM image of a selected particle showing the d(220) fringes. Inset shows the SAED pattern showing well defined rings. (b,c) The HRTEM images at different magnifications confirming the granular morphology of the catalyst.

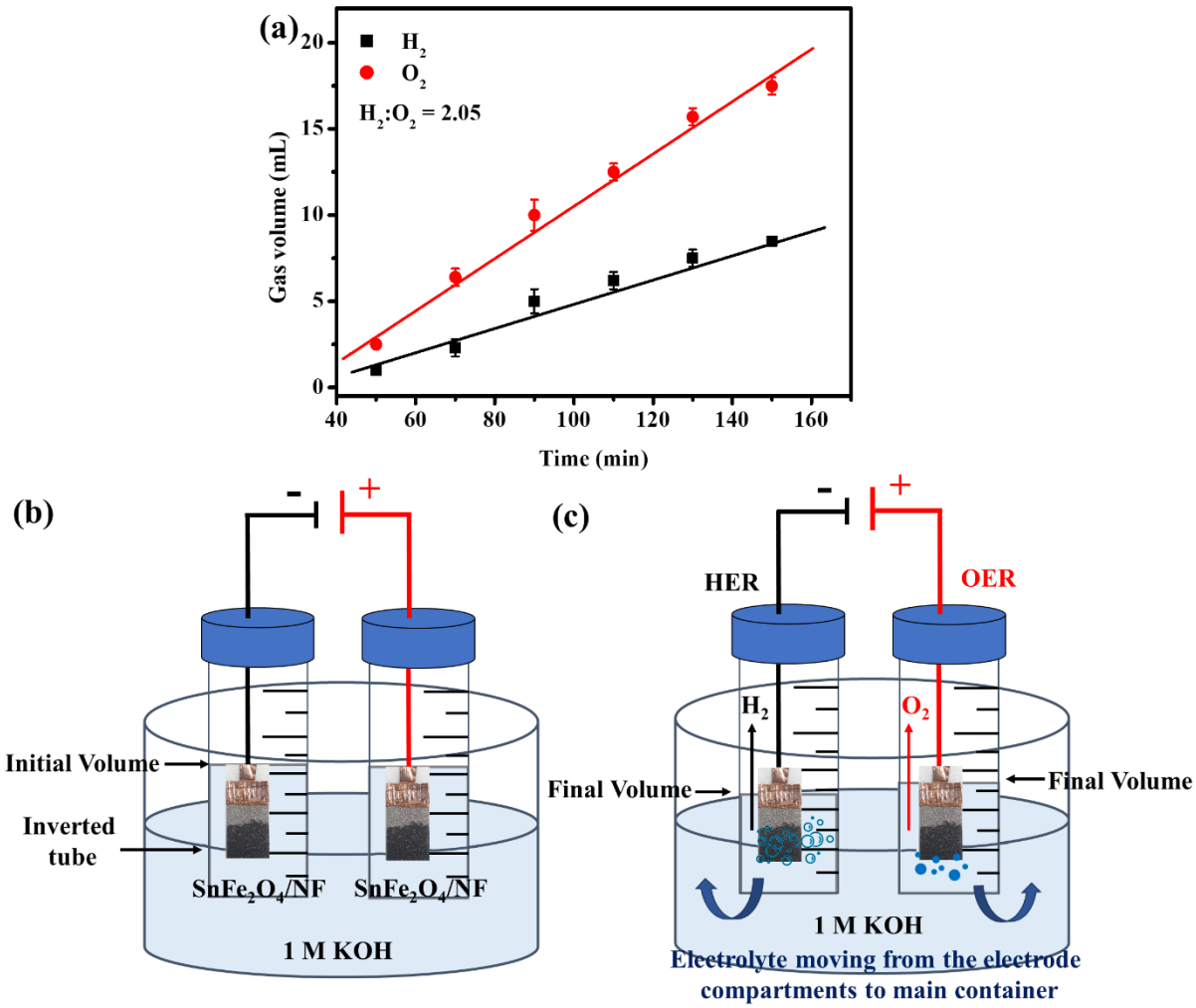

Figure S24. Long term electrolysis of $SnFe_2O_4$/NF(-)//(+)$SnFe_2O_4$/NF in a closed cell setup for 150 minutes. (a) The experimental ratio of evolved H_2:O_2 is in good accordance with the theoretical ratio of 2:1. (b) A schematic representation of self-customized setup for calculating the Faradic efficiency

of the catalyst (c) Schematic showing the decrease in electrolyte level due to gases produced during long-term electrolysis.

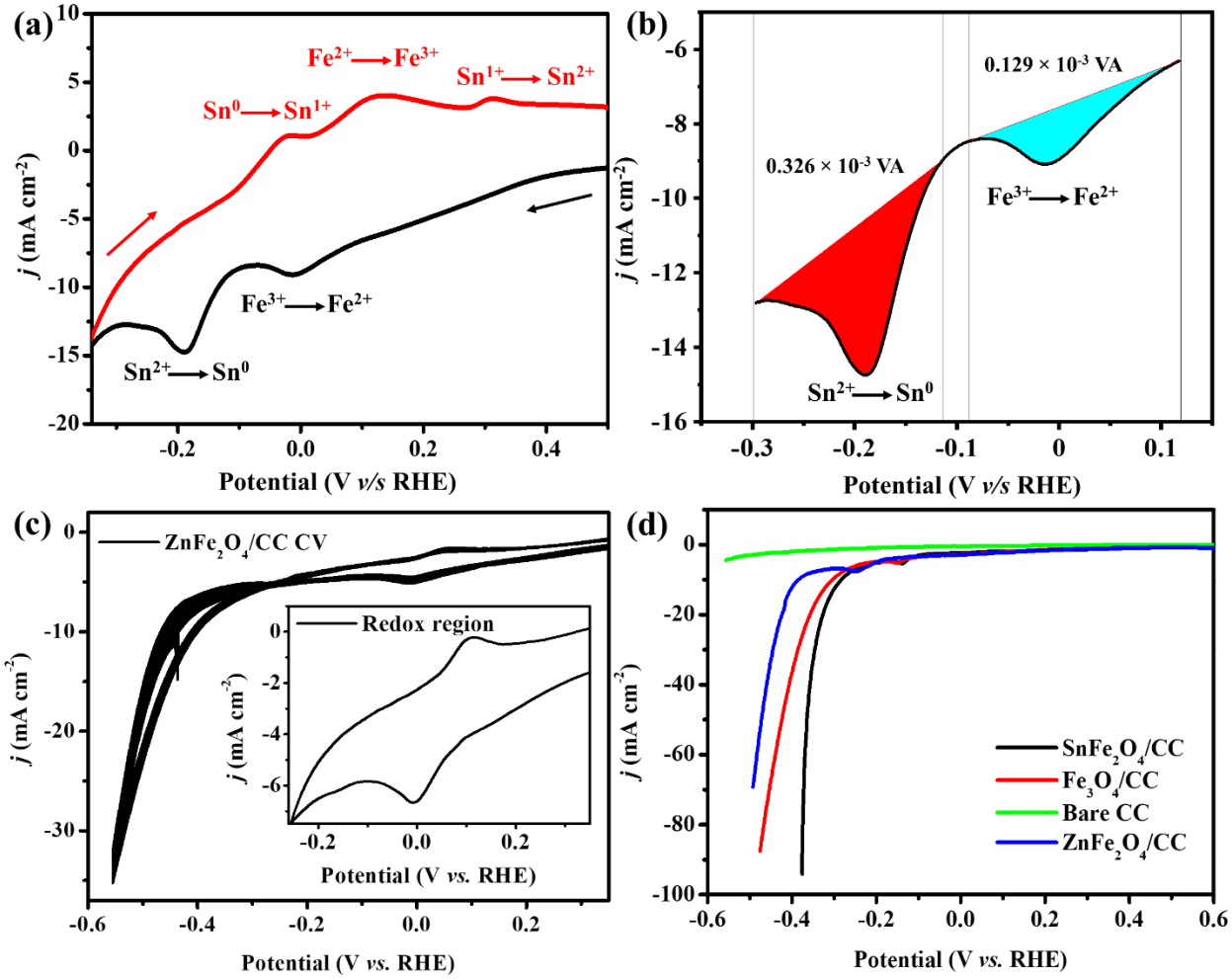

Figure S25. (a) The magnified $SnFe_2O_4$/CC CV cycle showing redox behaviour of Sn and Fe. (b) The redox region from the CV cycle showing the surface area for the peaks corresponding to the reduction of Fe and Sn. (c) $ZnFe_2O_4$/CC showing the redox feature of Fe and Zn on an inert support. (d) Electrochemical HER polarogram of $SnFe_2O_4$ and other control reference materials on inert support.

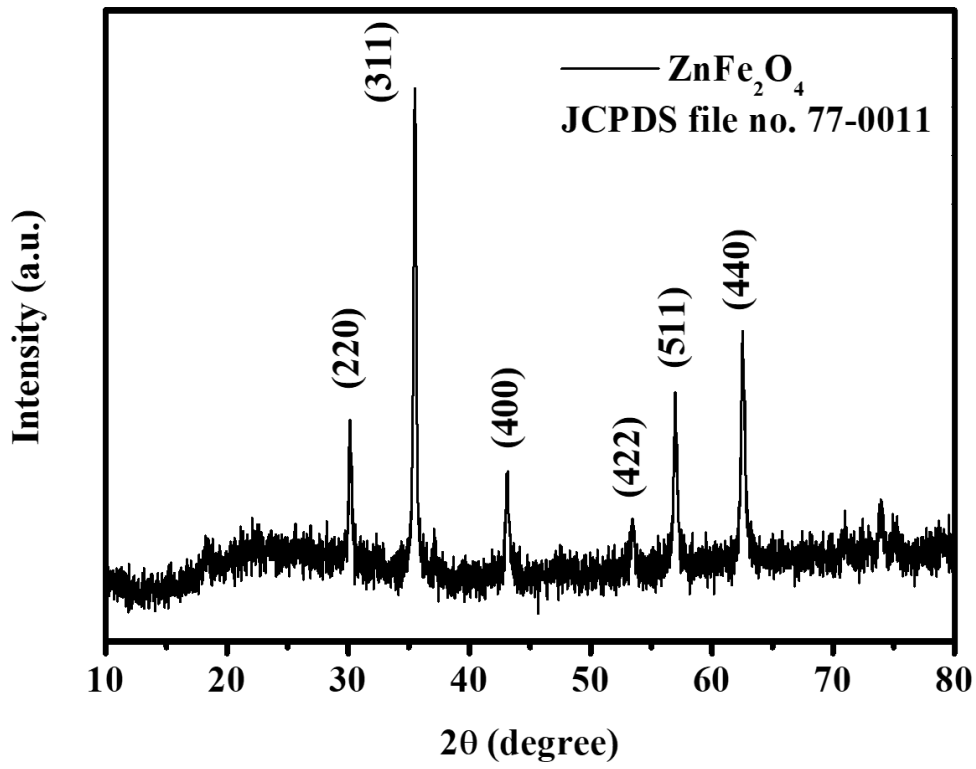

Figure S26. PXRD diffractogram of as -synthesized of $ZnFe_2O_4$ [24]

References:

1. F. L., L. B., X. R., W. D., Q. C., Z. W., L. J., J. D., Y. P. and Z. Y., *Adv. Funct. Mater.*, 2021, **31**, 2006216.
2. A. L. Patterson, *Phys. Rev.*, 1939, **56**, 978-982.
3. A. Rajput, M. K. Adak and B. Chakraborty, *Inorg. Chem.*, 2022, **61**, 11189-11206.
4. B. Chakraborty, R. Beltrán-Suito, V. Hlukhyy, J. Schmidt, P. W. Menezes and M. Driess, *ChemSusChem*, 2020, **13**, 3222-3229.
5. S. Kumaravel, P. Thiruvengetam, S. R. Ede, K. Karthick, S. Anantharaj, S. S. Sankar and S. Kundu, *Dalton Trans.*, 2019, **48**, 17117-17131.
6. S. C., Z. M. B., K. H., T. D., B. A., W. M., T. J., W. B., A. U.-P. and M. R., *Chem. Eur. J.*, 2021, **27**, 16990-17001.
7. S. C., T. J., T. D., J. J., A. U.-P. and M. R., *ChemElectroChem*, 2021, **8**, 227-239.
8. Y. H., L. Y., L. S., Z. Z., W. X., L. Y., W. Z., J. J. and M. J., *ACS Catal.*, 2017, **7**, 5557-5567.
9. Y. Q., L. C., W. Y., W. X., Z. X. and D. P., *J. Catal.*, 2018, **358**, 1-7.
10. O. G., W. F., H. K., H. N., Z. D., W. H., G. B., Y. H., L. L., L. H., S. Y. and W. H., *ACS Appl. Mater. Interfaces*, 2019, **11**, 3978-3983.
11. B. Debnath, S. Parvin, H. Dixit and S. Bhattacharyya, *ChemSusChem*, 2020, **13**, 3875-3886.
12. L. G., W. K., G. X., H. D. and L. J., *Electrochim. Acta*, 2016, **211**, 871-878.
13. O. K. F., A. S., S. S., Ö. F., H. J., A. C., L. J., W. H., S. W., M. M., L. T. and B. M., *Chem. Eur. J.* , 2017, **23**, 12443-12449.
14. S. Maitra, R. Mitra and T. K. Nath, *Curr. Appl. Phys.*, 2021, **27**, 73-88.
15. S. Karim, A. Chakraborty, S. Das, A. Banerjee and D. Das, *J. Electroanal. Chem*, 2022, **919**, 116465.
16. T. J., X. S., Z. H., C. H. and Z. G., *Electrochim. Acta*, 2021, **381**, 138199.

17. R. Appiah-Ntiamoah, A. F. Baye and H. Kim, *ChemElectroChem*, 2020, **7**, 3478-3486.
18. B. H., M. Y., K. M. R. and A. A., *Int. J. Hydrog. Energy*, 2022, **47**, 20129-20137.
19. S. S. S., B. T. K., K. S., K. A., M. R., B. K., N. S., D. H. N., L. S.-C. and K. S., *Nanoscale*, 2022, **14**, 10360-10374.
20. Y. F., C. X., W. M. and N. Y., *Electrochim. Acta*, 2019, **324**, 134883.
21. M. V., M. M., S. V., S. B. and M. S., *ACS Appl. Mater. Interfaces*, 2017, **9**, 13132-13141.
22. M. M., R. M., K. F., S. M., P. G. S., M. S. F. L. and D. U., *J. Phys. Chem. C*, 2019, **123**, 8304-8311.
23. B. Y. Geng, J. Z. Ma and J. H. You, *Cryst. Growth Des.*, 2008, **8**, 1443-1447.
24. P. Guo, L. Cui, Y. Wang, M. Lv, B. Wang and X. S. Zhao, *Langmuir*, 2013, **29**, 8997-9003.